Mon. Not. R. Astron. Soc. **000**, ??–10 (1997) Printed 3 April 1998 (MN LaTeX style file v1.3)

The stream impact region in the disc of WZ Sge

H. C. Spruit,[1] R.G.M. Rutten[2,3]
[1] *Max-Planck-Institut für Astrophysik, Postfach 1523, D-85740 Garching*
[2] *Netherlands Foundation for Research in Astronomy*
[3] *Royal Greenwich Observatory, Apartado de Correos 321, 38780 Santa Cruz de La Palma, Canary Islands, Spain*

Accepted xx Received ; in original form xx

ABSTRACT
We report the observation of new features in the spectrum of the Cataclysmic Variable WZ Sge. The disc eclipse is seen as a well-defined structure in the H_α line. From phases 0.25 to 0.5 an absorption feature of the same shape as the emission S-wave is seen in this line, but redshifted by ~200 km/s. Two possible interpretations of this feature are given, both of which imply that it originates at the impact point of the stream on the disc edge. In addition, evidence is found for substructure in the velocity map of the spot. Emission from line-emitting post-shock material, extending to about 60° downstream from the continuum hot spot is seen in the Doppler map in the form of a tail extending from the hot spot. A theoretical estimate shows that such a tail is to be expected as a consequence of the post-impact hydrodynamics of the stream. A new determination of the system parameters is made. They agree with those of Gilliland et al.; in particular, the data support a high primary mass. The variation of H_α surface brightness with distance from the primary is flatter, in the inner regions, than the $r^{-1.5}$ dependence found by Horne for other CV's in quiescence.

Key words: accretion discs – hydrodynamics – Cataclysmic Variables – stars: WZ Sge

1 INTRODUCTION

WZ Sge is one of the brighter cataclysmic variables. Its disc is partially eclipsed by the secondary, making it a good candidate for detailed studies of accretion discs in mass transfering binaries. The unusually long recurrence time of its outbursts, the light curve of these outbursts, and its low mass transfer rate make it comparable in many ways (van Paradijs and Verbunt 1984, Lasota 1996, Kuulkers et al. 1996) to the soft X-ray transients. Its quiescent spectrum is also very similar to that of the soft transients A0620-00 (Marsh et al. 1994) and GS2000+25 (Harlaftis et al. 1996). Because of the proximity of WZ Sge its disc can be studied in much more detail, at optical wavelengths, than the discs of the soft X-ray transient systems. This motivated the spectroscopic observations on which this paper is based. For reviews on the properties of WZ Sge, see Gilliland et al. (1986), Smak (1993), Warner (1995) and references therein.

2 OBSERVATIONS AND REDUCTION

About 700 spectra of WZ Sge were obtained with the 2.5 meter Isaac Newton Telescope using the Intermediate Dispersion Spectrograph on July 20–23 1995, during good seeing but with significant extinction by atmospheric dust. The spectra have a resolution of 2Å, covering the range 5800–7100Å on the EEV 1280×1180 CCD. About 80 spectra covering 4 orbits were taken with an integration time of 200s on the nights of July 20 and 21. The remaining spectra, on the nights of 21–23, were exposed for 30s. To correct for slit losses and variable (wavelength dependent) extinction, the field M dwarf located at 8" and position angle 100°.5 was exposed together with WZ Sge. We checked that H_α was in absorption in this dwarf in all spectra, making plausible that it is not a variable active star. Its spectrum was flux-calibrated with the standard BD+25 3941, and then used to flux-calibrate the individual spectra of WZ Sge in 6 continuum wavelength bands. The spectra, folded over orbital phase, are shown in figure 1.

A theoretical White Dwarf spectrum kindly provided by P. Bergeron (Bergeron et al. 1991, Bergeron 1993) for the temperature and gravity determined from HST observations by Sion et al. (1995) was scaled to match the observed HST UV flux and subtracted from the spectra in order to remove the broad absorption underlying the emission line. Maximum entropy Doppler maps (Marsh and Horne 1988) were then made, using the same algorithm as used previously (Spruit 1994) for eclipse mapping. The map for the combined 30 sec exposure data (fig. 1, left panel) is shown in figure 2. An expanded view of the hot spot region is shown in figure 4.

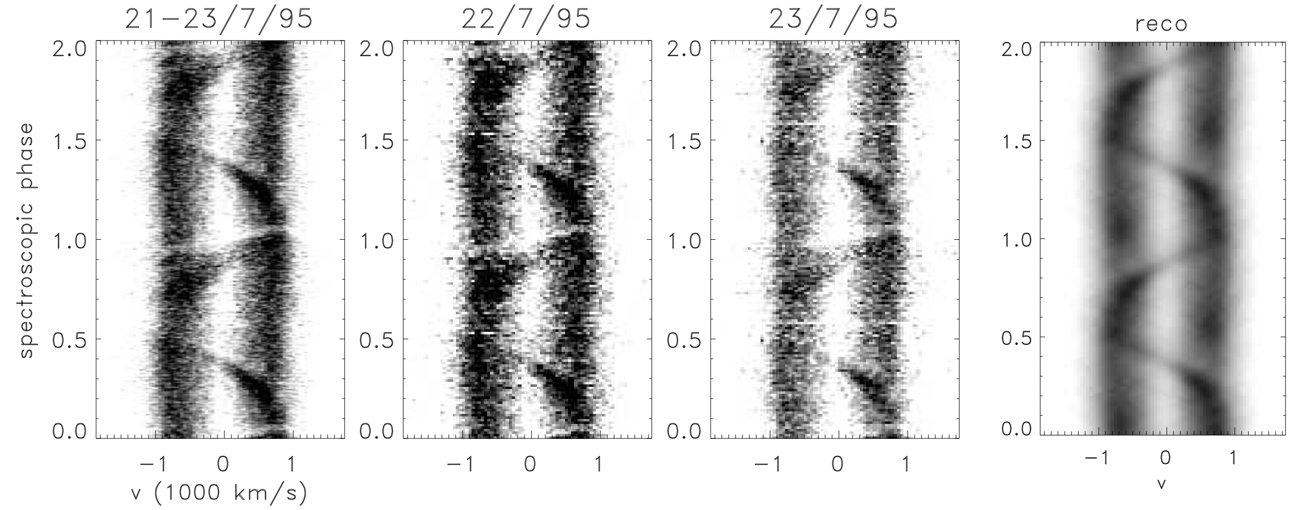

Figure 1. H_α spectra of WZ Sge. Left panel shows data covering about 12 orbits, obtained on three consecutive nights. Second and third panels show data from two of these nights separately. Phase is relative to inferior conjunction of secondary (see text). Note the absorption feature above the S-wave at phases around 0.25–0.5. Right panel: reconstructed spectrum from the Doppler map of the left-most panel.

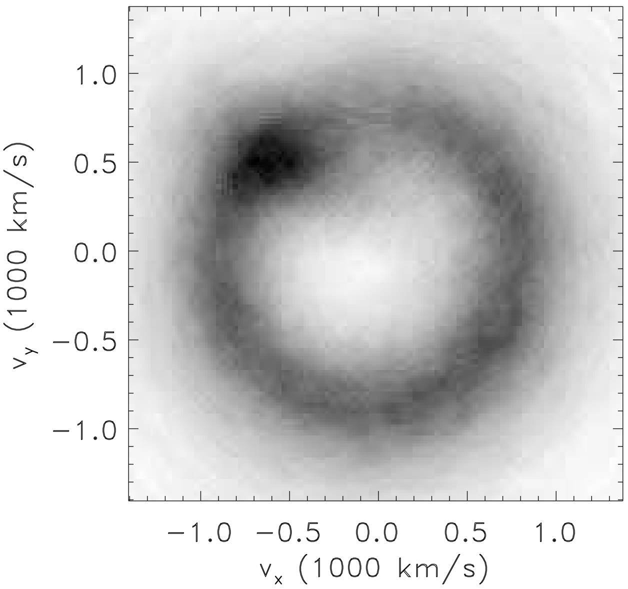

Figure 2. Doppler map from the leftmost spectrum of Fig.1. Note absence of emission at the expected velocity ($v_x = 0$, $v_y =$ 600km/s) of the secondary.

3 RESULTS

In addition to the classical S-wave, the spectrum shows some new features. The eclipse of the line profile is clearly seen as an inclined absorption feature around phase 0. The blue side of the line is eclipsed before the red side, as expected from an accretion disc in a mass transfering binary (e.g. Marsh et al. 1987, Marsh 1988). The phase of this feature determines the time of inferior conjunction of the secondary, relative to the conventional ephemeris (Robinson et al. 1978), which is based on the deepest point in the eclipse as seen in continuum light. In section 5 we measure this phase difference to be -0.041 ± 0.003. The phases in the axis in figure 1 and in the rest of the text are based on this determination of the spectroscopic zero point, i.e. they are shifted by -0.041 orbits with respect to the Robinson et al. ephemeris.

Evidence of eclipse in the line is seen up to velocities of about 1000 km/s. Together with the absence of an eclipse of the white dwarf, this puts constraints on the mass ratio and inclination of the system. This is discussed further in section 5.

On the red side of the line, the eclipse is more pronounced than on the blue side. This is expected because the eclipse of the hot spot coincides roughly with the eclipse of the red-shifted part of the disc. The deepest point of the eclipse in the red wing occurs at phase 0.055 ± 0.005. We can make the timing of the hot spot eclipse in the line more precise by noting that the observed emission from an axisymmetric disc is symmetric with respect to the transformation $\phi \to -\phi$, $v \to -v$ where ϕ is the phase relative to inferior conjunction and v the line-of sight velocity. This holds even including the eclipse of the disc by the companion. We can use this fact to subtract out all emission from the axisymmetric disc component. If $I(\phi, v)$ is the spectrum, the antisymmetric component

$$I_{\rm a}(\phi, v) \equiv I(\phi, v) - I(-\phi, -v) \tag{1}$$

isolates the emission from the hot-spot region. $I_{\rm a}$, integrated over the velocity range $700 < v < 1000$ km/s is shown in figure 3. Though the light curve of the hot spot emission is a bit noisy, the eclipse is clearly visible. We can compare it with the eclipse of the continuum light. Since our own continuum data are too noisy for the purpose, we use the light curve of Patterson et al (1996) which is from observations obtained, like our own data, in July 1995. These data were kindly provided in numerical form by Dr. Patterson, and are shown as the dashed line in fig. 3. Mid-eclipse of the continuum occurs at phase 0.041 ± 0.003. This corresponds exactly to phase 0 in the Robinson et al. (1978) ephemeris, showing that the phase of the hot spot eclipse is still a very stable feature of the light curve.

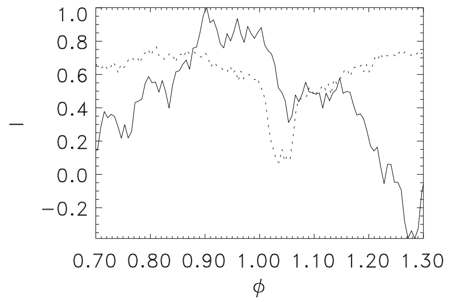

Figure 3. Light curve of the H_α emission from the hot spot (solid; see text), showing eclipse of the spot around phase 0.055. Dashed line shows continuum light curve, from Patterson et al. 1996. (Vertical scales arbitrary).

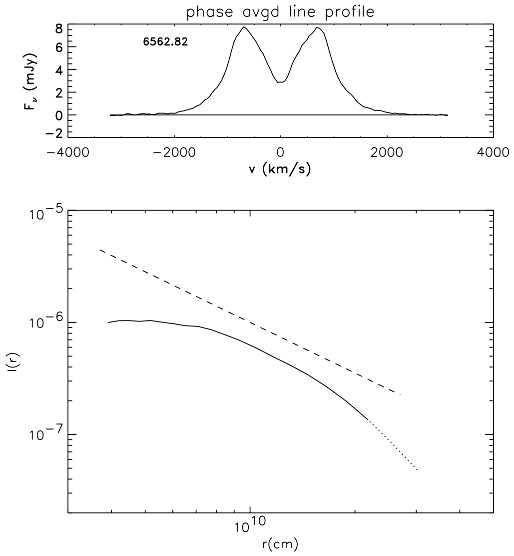

Figure 5. Top: phase-averaged line profile, with continuum and WD spectrum subtracted. Bottom: azimuthally averaged H_α emissivity (arbitrary units) vs. distance, from Doppler map. Broken line shows the -1.5 slope found by Horne and Saar (1991) in other CV's in quiescence.

The deepest point of the H_α eclipse appears to occur later than the continuum eclipse by about 0.015 orbits. It indicates that the hot spot as seen in H_α does not coincide exactly with the continuum hot spot, but somewhat downstream from it. In addition, the shape of the light curve suggests that some of the emission is eclipsed even later. This would indicate that the H_α hot spot is also more extended in azimuth than the continuum hot spot.

Another previously unseen feature is the absorption 'shadow' apparently tracking the S-wave between phases 0.25 and 0.5. It is seen on each of the four nights (compare left panel in figure 1 with the middle and right panels). Though only present at these phases, its behavior mimics that of the emission S-wave. For example, it looks broader on the red side than on the blue side. Its properties suggests that the feature is somehow physically related to the hot spot. Hints of this feature, which we shall call the 'S-wave shadow' are present in published data of some other systems, for example in the H_γ spectrum of U Gem in Marsh et al. (1990, their figure 2).

The Doppler maps of the hot-spot region show that the emission is distributed over an extended region in velocity space. This is shown in figure 4, which suggests a higher velocity component that is more extended in the azimuthal direction, and a component of slightly lower velocity which is less extended. This structure is visible in both maps, constructed from data obtained on different nights and with different time resolution (but similar total integration time). This shows that it is a relatively stable property of the emission region, and not an artefact of over-reconstruction of noise in the data.

Unlike in other systems (IP Peg: Marsh and Horne 1990, U Gem: Marsh et al. 1990, A0620-00: Marsh et al. 1994, GS2000+25: Harlaftis et al. 1996), there appears to be no emission whatsoever at the expected velocity of the secondary.

The radial distribution $I_\alpha(r)$ of H_α brightness can be deduced from the Doppler map by assuming that the rotation is keplerian. Transforming with this assumption the brightness in the Doppler map to surface brightness, and averaging azimuthally we get the profile shown in figure 5. The surface brightness in the innermost regions is determined by the far wings of the line profile, where the definition of the continuum and the subtraction of the primary spectrum introduce uncertainties. The phase-average of the line profile used in measuring $I_\alpha(r)$ is shown for comparison in figure 5. For dwarf novae in quiescence, Horne and Saar (1991) give evidence of a tendency for the Balmer emissivity to vary as $r^{-1.5}$, i.e. proportional to the local orbital rotation rate. Our measurement for WZ Sge differs somewhat from this trend, being significantly flatter than $r^{-1.5}$ in the inner regions. This may perhaps be related to the low viscosity in the disc of WZ Sge (as evidenced by the very long recurrence time of its outbursts). At very low viscosity, the mass transferred from the secondary is expected to accumulate as a 'ring' instead of forming a disc. The brightness distribution found here does not substantiate this picture, however. Though it is less 'disclike' than in some other CV's, it is definitely not a ring. On the other hand, the brightness in H_α is probably not a very good tracer of the mass distribution in the disc.

4 INTERPRETATION

4.1 The S-wave shadow

The densest part of the S-wave absorption feature has zero radial velocity with respect to the system at phase 0.42. If we use the Gilliland et al (1986) system parameters as a first guess, the disc radius would be about $0.31a$, and the mass ratio $q = 0.11$. The computed trajectory of the stream from the L_1 point then intersects the outer edge of the disc at an azimuth of 34° with respect to the line connecting the stars. Material in Kepler orbits at this azimuth has zero radial velocity at phase 0.41, close to the observed middle of the absorption feature. This suggests that the absorption S-wave originates at the impact point of the stream.

If the hot spot is located at the point where the computed stream meets the disc, the line of sight passes through the intervening accretion disc. An absorption feature will then occur if the optical depth to the hot spot around phase

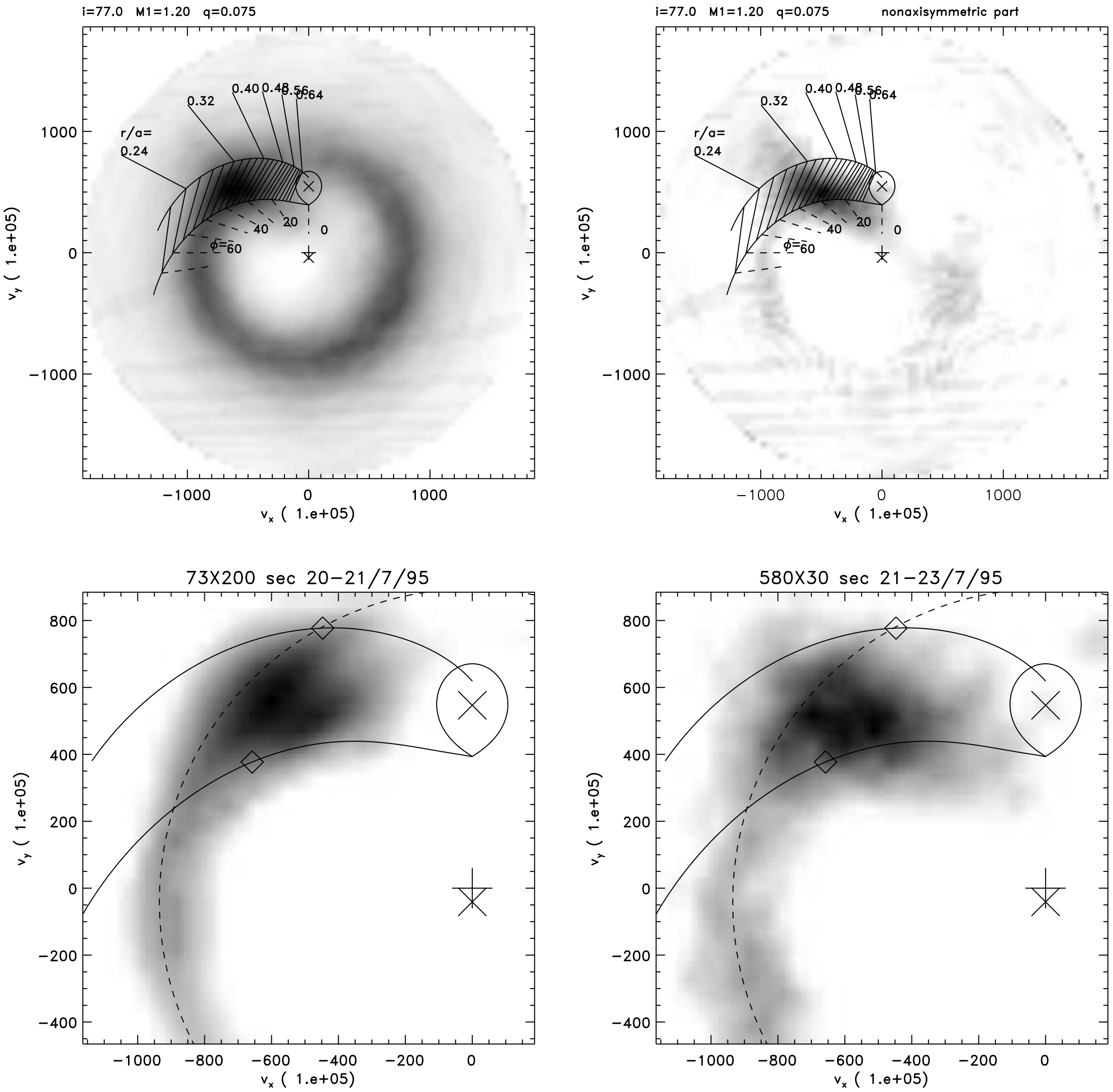

Figure 4. Top left: H_α Doppler map from all spectra combined, with stream path and Kepler velocity along stream (solid lines) for the system parameters derived here. Annotation gives radius and azimuth of stream relative to the primary. Top right: same map with the axisymmetric average taken out. Lower left: the hot-spot region from spectra with 200s time resolution. Axisymmetric average taken out to enhance the spot region. Lower right panel: same from 30s exposures. Diamonds give stream and Keplerian velocities at the stream impact point. Dashed line gives the projected velocity of the disc edge

0.4 is low in the continuum, but high in the line. This interpretation is consistent with the fact that the absorption is seen only between phases 0.25 and 0.5. In many high-inclination systems, the continuum light of the hot spot produces a single hump in the light curve, evidence that the hot spot is obscured by the disc when on the side of the disc facing away from the observer. In WZ Sge and its near-twin AL Com (Patterson et al. 1996), the orbital modulation is double humped (cf. Kato et al. 1996). This is interpreted (Robinson, Nather and Patterson 1978) as evidence that the disc in this system is sufficiently optically thin that continuum light from the hot spot is visible at all phases. Perhaps this happens only in systems of moderately high inclination ($\approx 77°$), such that the optical depth along the line of sight is not too large. The double humped nature of the light curve in WZ Sge is thus consistent with an interpretation of the S-wave shadow as originating at the stream impact point.

The precise physical cause is a bit more difficult to reconstruct. Continuum light absorbed by the intervening disc would have the right qualitative behavior, but quantitatively this does not explain the observation because the continuum at H_α is so weak in WZ Sge. The continuum eclipse shows that the flux from the continuum hot spot is only 0.4 mJy, compared with 9 mJy in the line peaks. Though absorption of continuum light from the hot spot may contribute some, the shadow must somehow involve the line photons themselves as well.

In the impact region, stream and disc material mix, with different velocities (Marsh et al. 1990). The impact region is thus geometrically limited, but emits H_α at a wide range of velocities (giving rise to the extended size of the hot spot region in the Doppler map). When seen through the intervening disc, emission at those velocities that match a (line of sight) velocity in the disc is absorbed. To see if this would produce an effective S-wave shadow, a simple model calculation was done, with results shown in figure 6. In the model, the hot spot is point-like, but has a broad distribution of velocities ('turbulence'), approximating the velocities seen in the hot spot region of the Doppler map of WZ Sge. The centroid of this velocity distribution is taken somewhat offset from the Kepler velocity $v_{\rm K}$ at the assumed hot spot position ($\delta v_x = -0.3 v_{\rm K}$, $\delta v_y = -0.1 v_{\rm K}$), as expected for mixing between disc and stream. The Doppler map of this model is shown in the left column of figure 6. At each orbital phase, the projected velocity of a Keplerian disc along the line of sight to the hot spot is determined, and all hot spot emission with velocities matching the line of sight velocity is assumed to be absorbed, up to a distance $r_{\rm a} = 0.3 r_{\rm disc}$ from the hot spot. This results is an absorption resembling the actual shadow qualitatively though not in detail (fig 6, lower left).

A second possibility is that the undisturbed disc in the region bordering the impact point actually has a *reduced* H_α brightness. Since the Kepler velocity at the hot spot position deviates from the mix of velocities in it, such reduced emission will appear *offset* from the hot spot emission in the Doppler map, as observed. Such reduced emission could be due to the intense UV emission from the hot spot, which might create a small fully ionized 'Strömgren sphere' around the hot spot. This possibility was tested by switching off the disc emission around the assumed hot spot position. This does indeed produce a pronounced S-wave shadow (lower right panel in fig 6).

While it is not quite clear which of these explanations is most appropriate, they have in common that in both the shadow approximately tracks the *Keplerian velocity at the stream impact point*. The phase at which the shadow passes through zero line of sight velocity thus marks superior conjunction of the hot spot in both interpretations. This is used to derive a constraint on the system parameters in section 5.

Apart from the absorption S-wave, there are other peculiarities in the spectrum that may be related to the effect of finite optical, depths. One is the disappearance of the S-wave around phase 0.6, which is not reproduced by the Doppler map (see figure 1). An interpretation of this disappearance in terms of finite optical depth effects has been given by Hantzios (1988).

4.2 Substructure in the H_α hot spot

The hot spot region is shown in more detail in figure 4. For comparison, these figures show also the stream path, the Keplerian velocity measured along the stream, the velocities of the centres of mass of primary and secondary (crosses), and the Doppler ghost of the secondary, for the system parameters derived in section 5.

A reasonable theoretical interpretation for the 'intermediate' velocities seen in the line emitting spot is found (Marsh et al. 1990) by considering the hydrodynamics at the impact point. At this point, there are two shocks, one in disc material and one in the incoming stream (Różyczka 1985). The postshock flows of both shocks are separated by a contact discontinuity, across which there is a difference in velocity. Emission from the postshock material would thus show up at two distinct velocities. Both these velocities would be intermediate between the stream velocity and the local Keplerian velocity.

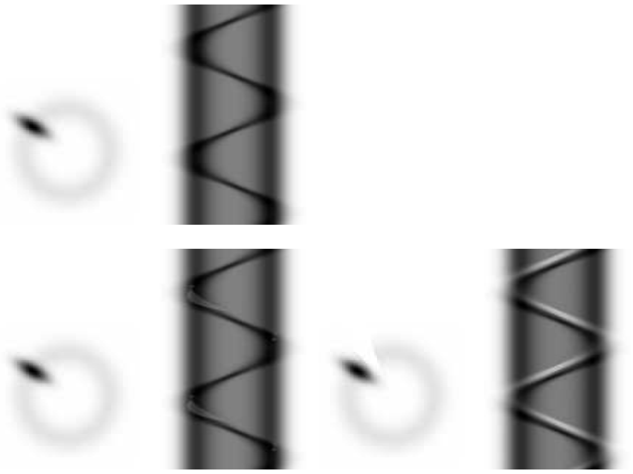

Figure 6. Model calculations for the S-wave shadow. Lower left: velocity map of the model and resulting spectrum assuming absorption by intervening disc. Lower right: assuming absence of disc emision near the hot spot position. For comparison the top left shows the map and spectrum without shadow modeling.

Mixing across this discontinuity by Kelvin Helmholtz instabilities is likely to occur, however, as is actually observed in hydrodynamical simulations (Różyczka 1985). If this is the case, it is not clear that the emission would show up in two separate velocity components. Dissipation of the relative kinetic energy may take some time, leading to a 'tail' of emission downstream from the impact region.

The situation is likely to be even more complicated, however, since it is not at all obvious that the main line emission originates at the impact point itself. The immediate postshock temperatures are of the order of a few million degrees, and the plasma does not emit in optical lines at such temperatures. The main optical line emission is expected during recombination, as the postshock material cools down. Since the gas, as it cools, travels in orbital direction, most of the H_α emission from the shock-heated gas is expected downstream from the impact point. In order to estimate how large this delay might be, we develop below some considerations on the hydrodynamics of the shock-heated gas. For a more extensive discussion of the processes involved see Meyer-Hofmeister et al. (1996) and Armitage (1997). The maps show clear evidence for this picture. In both data sets, a clear 'tail' is seen extending downstream from the hot spot area. Its width is much narrower than the broad range of velocities seen in the hot spot area itself. This supports the assumption that the tail is caused by material that has settled into approximate Keplerian motion downstream from the hot spot.

This interpretation of the tail provides a well defined velocity scale, which we use in section 5 as a constraint on the system parameters.

4.3 Post-impact hydrodynamics

With the known disc radius $r_{\rm d} = 0.37a = 1.7\,10^{10}$cm, a mass ratio $q = 0.075$, and a primary mass $M_1 = 1.2M_\odot$, the path of the stream from L_1 can be computed. The stream impacts the disc at velocity (velocity component normal to the disc rim) $v_1 = 530$km s^{-1}. Denoting pre- (post-)shock quantities with an index $_1$ ($_2$), the shock jump conditions (e.g., Landau and Lifshitz, 1959) then yield for the post-shock sound speed:

$$c_{\rm s2} = v_1[2\gamma(\gamma-1)]/(\gamma+1) \approx 0.56v_1 \approx 300\text{km s}^{-1}, \qquad (2)$$

where we have used $\gamma \approx 5/3$ since the ionization energy is small compared with the enthalpy behind the shock, and have ignored the gas pressure in the impacting stream. This post-shock sound speed is of the order 35% of the orbital speed (900 km/s) at the disc rim. The corresponding temperature is $4\,10^6$K. The hot post-shock gas is not in hydrostatic balance, and starts to expand to reach a new equilibrium. If cooling were ineffective, the expanding post-shock gas would reach a height $h = c_{\rm s}/\Omega \approx 5\,10^9$ cm. Evidence that some fraction of the gas actually reaches such heights have been found in U Gem (Mason et al. 1988) OY Car (Horne et al. 1994), UX Uma and RW Tri (Mason et al. 1997). For WZ Sge itself, the observation of an extended X-ray dip around phase 0.7 has also been interpreted as due to expansion associated with the stream impact (Richman and Patterson 1994, Richman 1996).

The expansion speed reached depends critically on the rate of cooling of the gas, however (Różyczka 1985). If the cooling time $t_{\rm c}$ is larger than the sound crossing time $t_{\rm s} = r_{\rm i}/c_{\rm s}$, where $r_{\rm i}$ the size of the impact region and $c_{\rm s}$ the post-shock sound speed, the expansion velocity will be of the order $c_{\rm s}$. If the cooling time $t_{\rm c}$ is shorter than $t_{\rm s}$, however, the pressure driving the expansion disappears before the full expansion speed $c_{\rm s}$ is reached. This turns out to be the case for the streams in most systems. The importance of cooling is thus governed by the ratio

$$s \equiv t_{\rm c}/t_{\rm s}, \qquad (3)$$

where $t_{\rm c}$ and $t_{\rm s}$ are given by

$$t_{\rm c} = l^2/\chi = l^2\frac{3}{16}\frac{\rho^2 c_p \kappa_{\rm R}}{\sigma T^3}, \qquad t_{\rm s} = l/c_{\rm s}. \qquad (4)$$

Here l is the size of the impact region, χ is the thermal diffusivity (cm^2/s), $\kappa_{\rm R}$ is the Rosseland opacity, c_p the specific heat, and σ the Stefan-Boltzmann constant. For $t_{\rm c}$ we have assumed that the cooling region is optically thick (see below). Because of the strong temperature dependence of $t_{\rm c}$, s turns out to be small at the immediate post-shock temperature of $4\,10^6$K. Thus, the postshock region quickly cools down to some intermediate temperature before significant expansion can take place. During this cooling phase, the pressure in the post-shock region is kept at the value dictated by the ram pressure of the stream,

$$p_2 \approx \rho_1 v_1^2 = v_1\dot M/(\pi r_{\rm i}^2), \qquad (5)$$

where $\dot M$ is the mass transfer rate and $r_{\rm i}$ the radius of the stream (assumed circular in cross-section). The post-shock temperature under the influence of cooling can then be estimated by setting $s \approx 1$. With $c_p \approx 5/2\mathcal{R}/\mu$ (valid for an ideal gas with $\gamma = 5/3$), and the length scale l equal to the stream radius $r_{\rm i}$, this yields

$$1 = \pi^2\frac{2}{5}\frac{3}{16}\frac{\sigma}{\kappa_{\rm R}}\left(\frac{\mathcal{R}}{\gamma\mu}\right)^{1/2}\frac{T^{9/2}}{\dot M^2 v_1^2}r_{\rm i}^3. \qquad (6)$$

With $v_7 \equiv v_1/10^7$ etc. this can be written as

$$T_4 \approx 3\dot M_{15}^{4/9} v_7^{4/9} r_8^{-1/3}\kappa_{\rm R}^{2/9}. \qquad (7)$$

Applying this to WZ Sge, the radius of the stream at impact is of the order 1/2 of its value r_0 at the L$_1$ point, which is given by (e.g. Meyer and Meyer-Hofmeister 1983),

$$r_0^2 \approx 0.2c_{\rm s0}^2/\Omega_{\rm orb}^2, \qquad (8)$$

where $\Omega_{\rm orb}$ is the binary orbital frequency. This gives $r_{\rm i} \approx 10^8$ cm. For $q = 0.09$, a white dwarf mass of 0.7 M$_\odot$, a disc radius $r_{\rm d}/a = 0.34$, and a mass transfer rate $\dot M_{15} \approx 1$ we find that the normal component of the impact velocity is $v_1 \approx 5.2\,10^7$, and the ram pressure $p_2 \approx 3\,10^6$. At the expected temperatures around $T_4 = 7$, this implies a density of the order $4\,10^{-7}$. With standard opacity tables for solar composition, this gives $\kappa_{\rm R} \approx 50$ cm^2/g, and (7) gives $T_4 \approx 7$.

Thus, the postshock gas cools down to a temperature of the order 70 000K, after which the cooling time becomes longer than the sound crossing time, in part because of the large (9/2) temperature dependence in (6), in part because of the rapid increase of the opacity due to partial H ionization. A phase of adiabatic expansion then sets in until the gas has mostly recombined and becomes transparent again. This happens at a temperature of the order 8000K. The speed of expansion is the sound speed at the end of the rapid cooling phase, i.e. corresponding to $T \approx 7\,10^4$. Denoting conditions at the beginning of the expansion phase by an index $_0$, we have $c_{\rm s0} = 3\,10^6$. The size of the expanding region varies with time as $l = l_0 + tc_{\rm s0}$. Assuming approximately isotropic expansion, the temperature in the expanding region varies as

$$T \sim \rho^{\gamma-1} \sim l^{3-3\gamma}. \qquad (9)$$

Taking $\gamma \approx 4/3$ as a representative number for the partially ionized gas, the temperature has decreased to 8000 K after a time $t \approx 200$s. With the orbital frequency $\Omega_d \approx 6\,10^{-3}$s^{-1} at the disc rim, this corresponds to an angle traveled by the expanding gas of the order $\Delta\phi \sim 60°$.

This estimate is rather approximate, but suggests the order of magnitude to be expected from a more detailed radiative hydrodynamical calculation. The main conclusion is that the hot spot is expected to be followed (in the orbital sense) by an extended 'tail' with strong H$_\alpha$ emission. Since the ionized matter has not yet recombined, the emission is expected to start only after having traveled some distance in orbital direction. No H_α emission is to be expected at the keplerian velocity at the stream impact point itself.

In this estimate, we have assumed that the post-shock region is optically thick so that a diffusion appoximation and a Rosseland opacity can be used. With the numbers derived we can now check on the consistency of this assumption. With a characteristic size $l \approx r_{\rm i}$, the optical depth of the region is

$$\tau \approx \frac{\kappa_{\rm R}\dot M}{\pi r_{\rm i} v_1} = 0.3\kappa_{\rm R}\dot M_{15} r_8^{-1} v_7^{-1}. \qquad (10)$$

With $v_7 = 3$ and $\kappa_{\rm R} = 50$, this yields $\tau = 5$ at the beginning of the expansion phase. Because the opacity increases during the subsequent adiabatic cooling, the optically thick

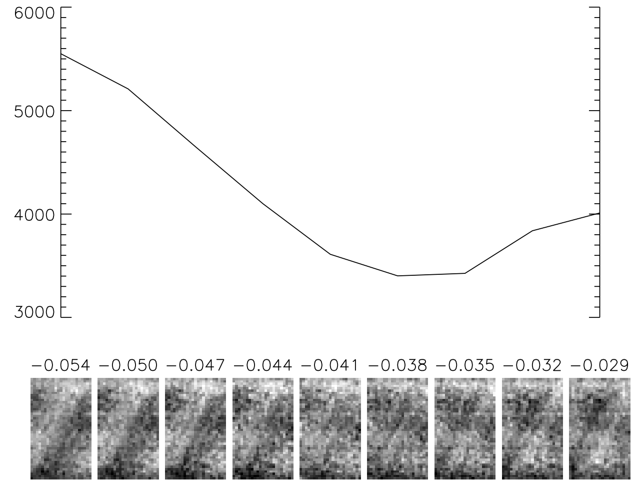

Figure 7. Determination of the phase ϕ_0 of inferior conjunction of the secondary from the disc eclipse. Images show the antisymmetric part of the region in the H_α-spectrum around the eclipse ($\Delta\phi = 0.14$), for 9 values of ϕ_0 (with respect to the Robinson et al. ephemeris). The disc eclipse feature is minimized at $\phi_0 = -0.041 \pm 0.003$. Curve on top shows the variation of the RMS value of the 9 images.

limit applies there. During the initial cooling phase, however, the assumption of optically thick cooling is less well justified. One might use an optically thin cooling formula instead. The conclusion, however, that fast initial cooling to a temperature around $6\,10^4$K takes place probably remains valid.

4.4 Consistency test

With this identification, the higher-velocity component of the hot spot follows an approximate Kepler orbit at the disc rim. The position of this component in the Doppler map then predicts the phase at which it will be eclipsed, which we can compare with the observed eclipse of the hot spot component (figure 3).

The peak of the higher-velocity component occurs around $v_x \sin i = -700, v_y \sin i = 520$ km/s (figure 4), corresponding, for a Keplerian orbit, to an azimuth of 53° from the axis connecting the stars. With a disc size $r_{\rm d}/a = 0.37$, mid-eclipse of this location is at $\phi = 0.057$. Within the uncertainties, this agrees with the observed phase (0.055) of the deepest point in the eclipse of the H_α hot spot (see light curve in figure 3). The tail seen extending from the hot spot area in the Doppler map (figure 4) would be eclipsed somewhat later, up to phase 0.060. This is consistent with the width of the H_α hot spot eclipse light curve.

In this way, we have demonstrated the internal consistency of the H_α hot spot eclipse with the appearance of the hot spot region in the Doppler map and the disc radius inferred from the absorption-S-wave.

5 SYSTEM PARAMETERS

We begin with the determination of the phase of inferior conjunction of the secondary. This quantity has not been determined before, mostly because the white dwarf is not eclipsed. The variations in the line profile during the eclipse of the disc seen in figure 1 can be used for a fairly accurate measurement.

For an axisymmetric disc, the eclipse produces an absorption feature that is point symmetric in the trailed spectrum. The feature therefore disappears in the antisymmetrised spectrum $I_{\rm a}(\phi, v) \equiv I(\phi, v) - I(-\phi, -v)$, where ϕ is the orbital phase relative to inferior conjunction. An error in the assumed phase ϕ_0 of inferior conjunction will show up in this antisymmetrised spectrum as a dark and a light image of the disc eclipse next to each other. By minimizing this easily recognizeable artefact the correct phase can be measured. This is shown in figure 7. From visual inspection of the sequence of antisymmetrised images for different assumed values we find $\phi_0 = -0.041 \pm 0.003$. A more quantitative method is to measure the RMS value of the antisymmetrised image, which has a minimum at the correct phase. This is shown in the curve on top of the sequence of images in figure 7. This curve suggests a slightly larger value for ϕ_0 than the visual determination, by about 0.004. A deviation from exact point symmetry occurs from of the presence of the hot spot, affecting the measurement of ϕ_0 somewhat. Because this effect is more easily 'filtered out' by human pattern recognition, we prefer our visual determination of ϕ_0.

The relevant system parameters are the primary mass M_1, the disc radius $r_{\rm d}$, the mass ratio q and the orbital inclination i. We have the following observational constraints on these parameters:

1. primary not eclipsed

The continuum light curve shows that the WD is not eclipsed. Taking into account the finite size of the primary (with a theoretical mass-radius relation) and the Roche geometry, this gives, for q and M_1 given, an *upper* limit on the inclination:

$$i < F_1(M_1, q). \tag{11}$$

2. maximum eclipsed velocity

The disc eclipse feature in the spectrum can be traced, both in the blue and in the red wing, up to an absolute line-of sight velocity of at least

$$v_{\rm m} = 900 \quad \text{km/s}. \tag{12}$$

Because of the noise in the data, it can not be excluded that even higher velocities are also eclipsed, so that we regard (12) as a lower limit. Assuming that the orbital velocities vary with distance as $r^{-1/2}$, and using the eclipse geometry, this determines a *lower* limit on the inclination:

$$i > F_2(M_1, q). \tag{13}$$

There is more information contained in the disc-eclipse feature than just the maximum velocity, and this could be used for improved constraints on inclination and primary mass. Somewhat better signal-to-noise would be needed, however, for a meaningful analysis of this kind.

3. radial velocity amplitude of the primary

We determine this quantity from the Doppler map, as

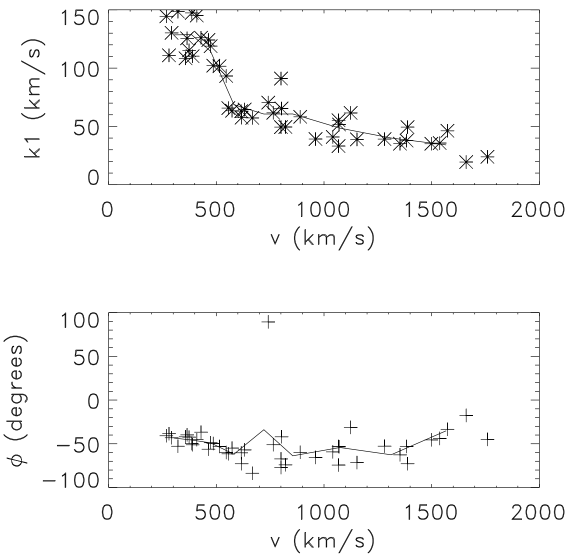

Figure 8. Radial velocity of the primary as measured from the Doppler map. Upper curve shows the amplitude K_1 as a function of the position in the line profile, lower curve the phase.

the offset from the origin of the centre of the ring of emission (due to the disc). Within rings centred at an assumed velocity (K_x, K_y) and with width Δv, the rms deviation of the intensity distribution from the average in the ring is measured, and minimized with respect to K_x and K_y. In doing this, the area in the map containing the hot spot is excluded, so that the measurement is done on the disc emission only. The process is repeated for a number of different radii and widths of the rings. The result is shown in figure 8, in the form of amplitude and phase of the K-velocity vector. As expected, the scatter in the points is smallest in the wings of the line (1000–1500 km/s), where we find $K_1 = 40\pm 10$ km/s. The phase of the K-velocity, which should be zero, is off by about 50°, as is usual in this kind of measurement in CV's (for a discussion see section 2.7.6 in Warner 1995). This introduces some doubt about the value of this determination. We decided to keep this measurement as a constraint, since it is not the only one influencing the secondary mass, and its consistency with the other constraints can be tested. Our value of K_1 agrees within the errors with that of Gilliland et al.

4. continuum hot spot eclipse phase

Since the conventional ephemeris is based on the continuum eclipse of the hot spot, the hot spot eclipse phase relative to inferior conjunction is:

$$\phi_c = 0.041 \pm 0.003, \tag{14}$$

5. continuum hot spot eclipse width

From Patterson's continuum light curve (see fig 3) we determine an eclipse width of

$$\Delta\phi_c = 0.06 \pm 0.02. \tag{15}$$

6. hot spot azimuth

From the absorption S-wave, discussed in section 4.1, we find that the hot spot is at superior conjunction at phase 0.42, and we estimate the error in this number to be 0.01. This means that the hot spot, as seen from the primary, is located at an azimuth of

$$\theta_c = 0.08 \times 360 = 29^\circ \pm 4 \tag{16}$$

ahead of the secondary.

7. projected orbital velocity at the hot spot

The hot spot region itself contains a mixture of velocities. As argued above, however, the 'tail' of emission extending from it is probably due to material orbiting at the outer edge of the disc, at the Keplerian velocity. The velocity amplitude of the tail, measured as its radius from the position of the primary in the Doppler map (determined by the measured value of K_1), is

$$K_s = 900 \pm 70 \quad \text{km/s}. \tag{17}$$

These measured numbers are compared with predicted values as a function of the system parameters (r_d, M_1, q, i). The input for this calculation are the known orbital period and the usual model assumption of a Roche geometry and the assumption that the hot spot lies on the orbit of a particle starting at L_1.

A probability distribution for the system parameters was constructed from the constraints as follows. For constraints 3–7, we assume that the measurement uncertainty is normally distributed. If the quantity measured in constraint number k is f_k, ϵ_k its uncertainty, and $F_k(r_d, M_1, q, i)$ the value calculated from the model, the probability that a given parameter set (r_d, M_1, q, i) agrees with the data is proportional to the function g_k, defined by

$$g_k = \exp[-(F_k - f_k)^2/\epsilon_k^2]. \tag{18}$$

For constraints 1 and 2, which only provide limits, we define the function g_k as unity when the condition is satisfied and zero if it is not.

Since the constraints are all independent, the joint probability under several constraints is proportional to the product of the corresponding g_k. The functions g_k are computed on an equidistant grid in the parameters. We found this more convenient and efficient than a Monte-Carlo method.

Since there are more constraints than parameters, different combinations of the constraints give different confidence intervals for the parameters. This is shown in figure 9. The upper two panels show the confidence intervals for M_1, q and i from the three constraints that are independent of the disc radius (numbers 1,2,3). They show contours of projections onto the (q, M_1) and (q, i) planes of the joint probability $g_a \equiv g_1 g_2 g_3$. The middle row gives the contours for the same parameters from the r_d-dependent constraints 4–7. One sees that the second set gives tighter confidence intervals, but otherwise is compatible with the first set. The lower row gives the contours, of projections onto the (q, M_1) and (r_d, i) planes, of the joint probability F from all constraints, $F \equiv \prod_{k=1,7} g_k$.

5.1 Result

From the projection of the distribution onto the four axes, we obtain the following values for the system parameters: $r_d/a = 0.37 \pm 0.03$, $M_1 = 1.2 \pm 0.25$, $q = 0.075 \pm 0.015$, $i = 77^\circ \pm 2^\circ$ (1-σ uncertainties).

The maximum of each of the g_k is unity, but since

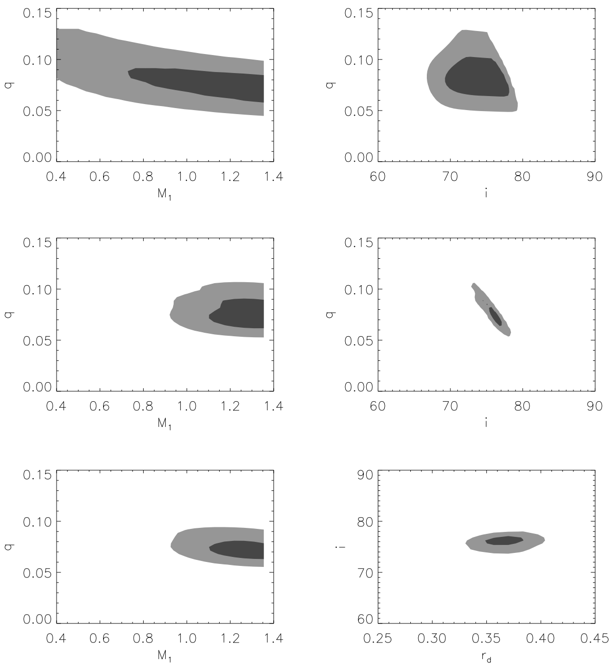

Figure 9. System parameters determined from 7 observational constraints. Top row: probability contours (67 and 90%) of M_1, q and i using the three observational constraints that do not involve the disc radius. Middle row: same using the 4 remaining constraints. Lower row: contours for $r_{\rm d}$, M_1, q and i using all 7 constraints.

there are more constraints than parameters, the maximum of F over all values of the parameters is less than unity. The actual value of $\max(F)$ is an indication of the degree compatibility of the constraints. The data in figure 9 have $\max(F) = 0.87$, sufficiently close to unity that the constraints can be called mutually consistent. In particular, the two independent sets of constraints shown in figure 9 both indicate a high primary mass and a mass ratio around 0.07.

For completeness, we mention the γ-velocity measured from the data. An error in the assumed value of γ is accurately measured by subtracting the input spectrum from the spectrum reconstructed from the Doppler map. By minimizing the artefacts in this difference map (bright/dark shadows), we find $\gamma = -71 \pm 3$km/s.

5.2 discussion: primary mass determinations, distance of WZ Sge

The values found here are in agreement, within the errors, with those of Gilliland et al., though we believe we have sharpened the accuracy, in particular on M_1 and q. The low value $M_1 = 0.45$ favored by Smak (1993) cannot be reconciled with our Doppler map. A high primary mass is also indicated by the high velocities that are seen to be eclipsed in the line profile, though this constraint is less strong.

A low primary mass (0.6 $M_\odot$) was also preferred by Sion et al. (1995) in their analysis of the HST UV spectrum. Due to the rather strong degeneracy between the temperature and the gravity derived from this spectrum, the uncertainty in $\log g$ is probably substantial (Sion et al. give $T = 14900$ K, $\log g = 8.0$, without error bars). Our determination $M_1 = 1.2$ corresponds to $\log g = 9.0$. Extrapolating from table 2 in Sion et al., the best-fit temperature from the HST spectrum at this $\log g$ would be 17800 K. The reduced χ^2 of the fit (1794 degrees of freedom) would increase from 1.515 to about 1.6. While such an increase in χ^2 would be significant in itself, the rather high reduced χ^2 at best fit shows that there are significant features in the HST spectrum that have not been fitted. It is therefore hard to assign a significance level to the degree of disagreement of a $\log g = 9$ fit.

Looking for possible causes of the discrepancy in M_1, we note that our value is determined most strongly by our interpretation of the hot spot tail in the Doppler map, though the other observational constraints (figure 9, top left) point in the same direction. If our interpretation that this tail represents material orbiting at the Kepler rate is discarded, the range of M_1 compatible with the data would increase significantly. If, instead of taking the velocity of the tail, one takes the mean velocity of the hot spot, $v \sin i = 820$ km/s, one would get $M_1 = 0.9$. Our Doppler map, however, shows unequivocally that the hot spot has a rather large intrinsic extent in velocity. We have shown that this is to be expected from the hydrodynamics of stream impact on the disc. Hence some form of interpretation is needed to associate one of the components in the map with an orbital velocity. The center of gravity of the spot in the Doppler map, or of the S-wave taken directly from the spectrum would not, a priori, constitute a more reliable association. If our interpretation is correct, the orbital velocity at the disc edge is somewhat larger than the mean of the hot spot in a Doppler map would indicate, namely $v \sin i = 900$ km/s, or $v = 925$ km/s. A value of M_1 as low as 0.6 would correspond to an orbital velocity at the disc edge of $v \sin i = 714$km/s, which is clearly contradicted by our Doppler map. Such a value corresponds, incidentally, to the separation of the peaks in the average line profile (figure 5). As we have argued, however, the peak separation is a very misleading quantity which seriously underestimates the orbital velocities.

If our interpretation of the emission tail is correct, and WZ Sge representative in this respect, determinations of M_1 relying on the S-wave in other CV's would have to be revised upwards as well. Masses determined from the mean velocity of the hot spot (fits to the S-wave for example) would have to be increased by 30%.

Except for the uncertainty in the WD radius, the HST spectrum provides the best information on the distance of WZ Sge, since the WD dominates the spectrum and peaks in the UV. With $\log g = 9$ and $T = 17800$, the scale factor extrapolated from table 2 in Sion et al. would be 0.0137. With their formula (1) and $R_1 = 3.9 \times 10^8$ this gives a distance of 48 pc.

ACKNOWLEDGEMENTS

We thank Keith Horne for constructive criticism and several suggestions which helped to improve the presentation of the data. We also thank Erik Kuulkers and Steve Howell for their comments on the text. We thank the anonymous referee for his criticism and for pointing out an error in our distance determination. We thank Dr. Patterson for making available the continuum light curve of figure 3 in numerical form. HCS thanks Brian Warner for discussions on observations and theory of CV's. His work was done in the context of the research network 'Accretion onto compact objects and protostars' (EC Human Capital and Mobility Grant CHRX-CT93-0329). The Isaac Newton Telescope is operated on the island of La Palma by the Royal Greenwich Observatory in the Spanish Observatorio del Roque de los Muchachos of the Instituto de Astrofisica de Canarias.

REFERENCES

Armitage P.J., 1997, preprint, astro-ph/9707354
Bergeron P., Wesemael F., Fontaine G., 1991, ApJ 367, 253
Bergeron P. 1993, in White Dwarfs: Advances in Observation and Theory, ed. M.A. Barstow, Dordrecht: Kluwer, p.267
Gilliland R.L., Kemper E., Suntzeff N., 1986, ApJ 301, 252
Hantzios P.P., 1988, PASP 100, 1188
Harlaftis E.T., Horne K., Filippenko A.V., 1996, PASP 108, 762
Horne K., Saar S.H., 1991 ApJ 374 L55
Horne K., Marsh T.R., Cheng F.H., Hubeny I., Lanz T., 1994, ApJ 426, 294
Horne K., Marsh T., 1986, MNRAS 218, 761
Kato T., Nogami D., Baba H., et al., 1996 PASJ 48, L21
Kuulkers E., Howell S.B., van Paradijs J., 1996, ApJ 462, L87
Landau L.D., Lifshitz E.M., 1959, Fluid Mechanics, Pergamon Press
Lasota J.P., 1996, in Compact stars in binaries (IAU Symp. 165), eds. J. van Paradijs, E.P.J. van den Heuvel, E. Kuulkers, Kluwer Dordrecht, p.43
Marsh T.R., 1988, MNRAS 231, 1117
Marsh T.R., Horne K., Shipman H.L., 1987, MNRAS 225, 551
Marsh T.R., Horne K., 1988, MNRAS 235, 269
Marsh T.R., Horne K., Schlegel E.M., Honeycutt R.K., Kaitchuk R.H., 1990, ApJ 364, 637
Mason K.O., Cordova F.A., Watson M.G., King A.R., 1988, MNRAS 232, 779
Mason K.O., Drew J.E., Knigge C., 1997, MNRAS 290, 23
Meyer F., Meyer-Hofmeister E., 1983, A&A 121, 29
Meyer-Hofmeister E., Schandl S., Meyer F., 1996, in preparation
Patterson J., Augusteijn T., Harvey D.A., Skillman D.R., Thorstensen J., 1996, PASP 108, 748
Richman H.R., Patterson J., 1994, BAAS 185, 21.12
Richman H.R., 1996, ApJ 462, 404
Robinson E.L., Nather R.E., Patterson J., 1978, ApJ 219, 168
Różyczka M., 1985, Acta Astron. 38, 175
Sion E.M., Cheng F.H., Long K.S., Szkody P., Gilliland R.L., Hunag M., Hubeny I., 1995, ApJ 439, 962
Smak J., 1993, Acta Astron. 43, 101
Spruit H.C., 1994, A&A 289, 441
van Paradijs J., Verbunt F., 1984, in S.E. Woosley, ed., High Energy Transients in Astrophysics, AIP Conference Procs 115, p 49
Warner B., 1995, Cataclysmic Variable Stars, Cambridge University Press.